

## **4.0 Algebraic Turbulence Models**

### **4.1 Inner Eddy Viscosity Model**

Most of the earliest turbulence models were based on Prandtl's mixing length hypothesis. Prandtl<sup>1</sup> suggested that the eddy viscosity could be represented by

$$\mu_t = \rho L_m^2 \left| \frac{\partial u}{\partial y} \right| \quad (4.1)$$

The Prandtl mixing length relates the eddy viscosity to the local mean velocity gradient. The secret to successful applications of the mixing length hypothesis is to find some general method of defining the mixing length. Most algebraic models divide the boundary layer into an inner and outer region as described in Chapter 3. The inner layer includes the viscous sublayer, the buffer layer, and part of the fully turbulent log region. The outer layer includes the remaining part of the log layer and the wake region. The eddy viscosity in the inner layer follows Prandtl's form and is given by

$$(\mu_t)_{inner} = \rho L_m^2 |\Omega| \quad (4.2)$$

where the mixing length  $L_m$  is given by

$$L_m = \kappa y \left[ 1 - \exp\left(\frac{-y^+}{A^+}\right) \right] \quad (4.3)$$

where  $y$  is the distance normal to the wall,  $\kappa$  is the von Karmen constant, and the vorticity  $\Omega$  is defined as

$$|\Omega| = \left| \frac{\partial u}{\partial y} - \frac{\partial v}{\partial x} \right| \quad (4.4)$$

### **4.2 Cebeci-Smith Model**

Cebeci-Smith<sup>2</sup> suggested that the outer eddy viscosity be expressed as

$$(\mu_t)_{outer} = \rho \alpha u_e \delta^* \quad (4.5)$$

Here  $\alpha$  is usually assigned a value of 0.0168 for flows where the Reynolds number based on momentum thickness ( $Re_\theta$ ) is greater than 5000,  $\delta^*$  is the displacement thickness, and  $u_e$  is the velocity at the edge of the boundary layer. The final eddy viscosity is

$$\mu_t = \min[(\mu_t)_{inner}, (\mu_t)_{outer}] \quad (4.6)$$

This model is fairly simple, but it requires knowledge of the conditions at the edge of the boundary layer and the boundary layer thickness. These quantities are not always easy to calculate in complicated flows with a Navier-Stokes code since it is often difficult to define where the boundary layer edge actually occurs.

### **4.3 Baldwin-Lomax Model**

Baldwin-Lomax<sup>3</sup> developed a form of the outer eddy viscosity that did not require knowledge of the conditions at the edge of the boundary layer. This model has become quite popular for CFD applications. The eddy viscosity in the outer layer is defined as

$$(\mu_t)_{outer} = \rho K C_{cp} F_{wake} F_{kleb} \quad (4.7)$$

where  $F_{wake}$  contains the mixing length term and  $F_{kleb}$  is the Klebanoff intermittency factor. These terms are defined as

$$F_{wake} = \min\{y_{max} F_{max}, C_{wk} y_{max} U_{diff}^2 / F_{max}\} \quad (4.8)$$

The quantities  $F_{max}$  and  $y_{max}$  are taken from the maximum of the  $F$  function defined as

$$F(y) = y |\Omega| \left[ 1 - \exp\left(\frac{-y^+}{A^+}\right) \right] \quad (4.9)$$

and  $U_{diff}$  is given by

$$U_{diff} = \left( \sqrt{U^2 + V^2} \right)_{max} - \left( \sqrt{U^2 + V^2} \right)_{min} \quad (4.10)$$

The  $F$  function is calculated along a line normal to the wall. The  $F$  function for a typical attached boundary layer is shown in Fig. 4.1.

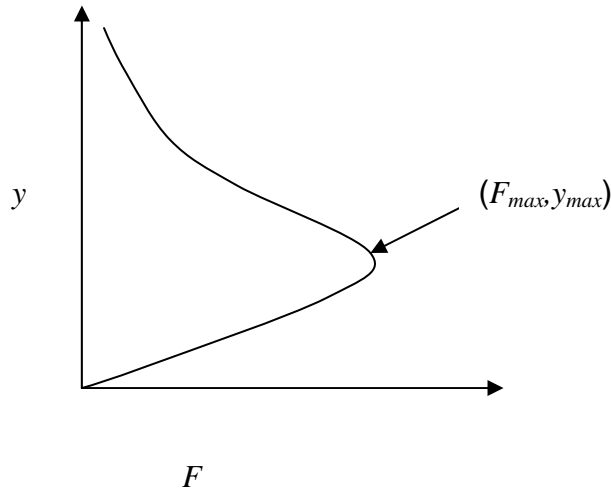


Figure 4.1 The  $F$  function (Eq. 4.9) for an attached boundary layer.

The Klebanoff intermittency factor<sup>4</sup> is given by

$$F_{kleb}(y) = \left[ 1 + 5.5 \left( \frac{C_{kleb} y}{y_{max}} \right)^6 \right]^{-1} \quad (4.11)$$

The final eddy viscosity is

$$\mu_t = \min[(\mu_t)_{inner}, (\mu_t)_{outer}] \quad (4.12)$$

The constants used in the Baldwin-Lomax model are

$$A^+ = 26, C_{cp} = 1.6, C_{kleb} = 0.3, C_{wk} = 1.0, \kappa = 0.4, K = 0.068 \quad (4.13)$$

Algebraic models work well for flows that can be characterized by a single length scale such as attached boundary layers or simple shear layers. The Baldwin-Lomax model determines the appropriate mixing length from the location of the peak in the  $F$  function. For simple flows there will only be one peak in the  $F$  function. In more complicated flows with multiple shear layers such as separated boundary layers or wall jets the  $F$  function will contain multiple peaks. When multiple peaks are present it becomes difficult to automatically choose the proper peak to use, if a single peak can be used to model the turbulent flow. Degani and Schiff<sup>5</sup> recommended a procedure to automatically select the first significant peak in the  $F$  function. This modification to the search procedure for the peak has been shown to improve the performance of the Baldwin-Lomax for high angle-of-attack flows with cross-flow separation.

#### **4.4 Wake and Jet Model**

The Baldwin-Lomax model has been modified for use in wakes and jets (Ref. 6). First,  $U_{diff}$  in Eq. 4.11 is redefined as

$$U_{diff} = \left( \sqrt{U^2 + V^2} \right)_{\max} - \left( \sqrt{U^2 + V^2} \right)_{y \max} \quad (4.14)$$

The exponential term in the definition of  $F(y)$  (Eq. 4.9) is set to zero yielding

$$F(y) = y|\Omega| \quad (4.15)$$

The  $F_{wake}$  function (Eq. 4.8) is redefined to be

$$F_{wake} = y_{\max} F_{\max} = \left( \frac{U_{diff}}{|\Omega|_{\max}} \right)^2 |\Omega|_{\max} \quad (4.16)$$

The  $y_{\max}$  location in Eq. 4.16 is defined to be the location where  $|\Omega|_{\max}$  occurs. Finally the Klebanoff intermittency factor  $F_{kleb}$  (Eq. 4.11) is rewritten as

$$F_{kleb} = \left( 1 + 5.5 \left( C_{kleb} \frac{|y - y_{\max}|}{\left( \frac{U_{diff}}{|\Omega|_{\max}} \right)} \right)^6 \right)^{-1} \quad (4.17)$$

This wake formulation will work for individual simple shear layers. If multiple shear layers are present, the user must partition the flow and apply the turbulence model to each shear layer individually. This can easily become impractical for complicated geometries.

#### **4.5 Algebraic Model Shortcomings**

The flow in a two-dimensional channel with a circular arc bump contraction can be used to demonstrate two shortcomings of the Baldwin-Lomax turbulence models. These shortcomings are the model's tendency to switch  $F_{\max}$  peaks and the lack of any transport terms in the turbulence model. Fig. 4.2 shows the geometry and the eddy viscosity contours for both the Baldwin-Lomax and Spalart-Allmaras turbulence models. The eddy viscosity predicted by the Baldwin-Lomax is seen to reduce itself almost to zero at the start of the bump. The Spalart-Allmaras one-equation transport turbulence model (discussed in the next section) predicts a much smoother distribution of eddy viscosity on the bump. The reason for the anomaly in the Baldwin-Lomax model can be seen in

Fig. 4.3. The location of the  $F_{max}$  peak moves very close to the wall at the start of the bump ( $x=0$ ) and rises back to its original level at the bump trailing edge ( $x=1$ ). The relative magnitude of the  $F_{max}$  peak is also shown in Fig. 4.3, and is seen to increase in the region of the bump. The eddy viscosity is proportional to the product of the distance of the peak off the wall and the magnitude of the peak, and is seen to decrease in the region above the bump because the  $F_{max}$  peak has moved very near the wall. The sudden switching of the  $F_{max}$  peak causes the turbulence level to be greatly reduced in the favorable pressure gradient region near the bump leading edge. If the Baldwin-Lomax model included transport terms, then the higher upstream values of eddy viscosity would be transported downstream at the beginning of the bump, and the Baldwin-Lomax predicted eddy viscosity distribution would not demonstrate the discontinuous behavior it shows here.

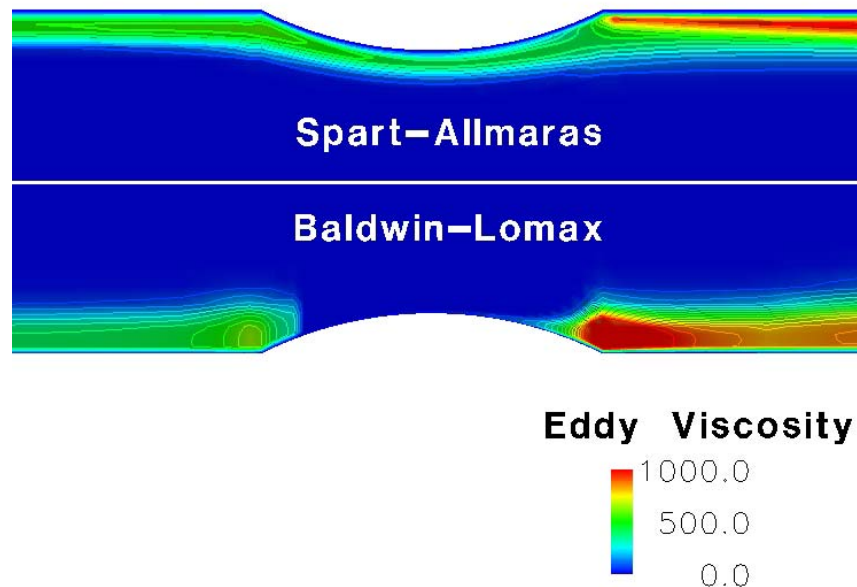


Figure 4.2 Eddy viscosity contours for a circular arc bump in a two-dimensional channel for two different turbulence models.

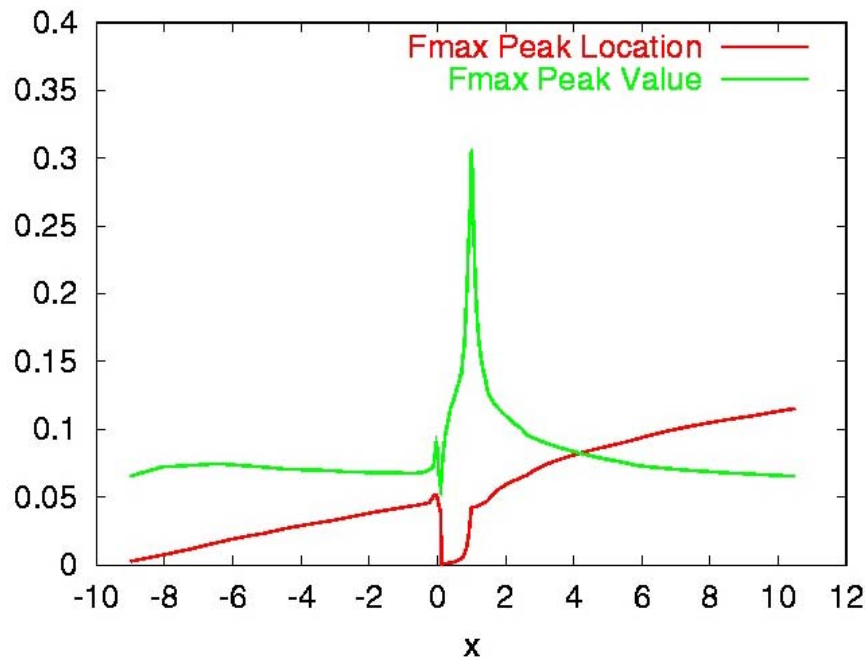


Figure 4.3 Distance above the wall of the  $F_{max}$  peak and the  $F_{max}$  value for a two-dimensional channel with a circular arc bump.

#### **4.6 Grid Sensitivity for a Flat Plate with Adiabatic Wall**

The initial wall spacing of the computational grid and the grid-stretching ratio (the ratio of the change in grid spacing normal to the wall) can affect the accuracy of the Baldwin-Lomax model. Figure 4.4 shows the sensitivity of the skin friction to initial wall spacing for a flat plate. The grid-stretching ratio was 1.2 for all these cases. The plots include the theoretical skin friction curves of White and of Spalding.

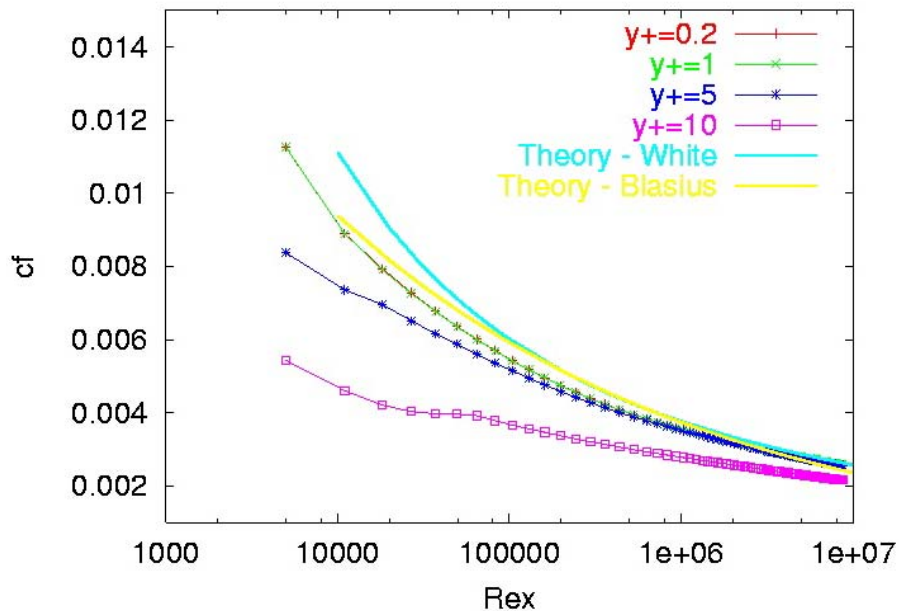


Figure 4.4 Flat plate skin friction predictions for the Baldwin-Lomax turbulence model for varying initial wall grid point spacings.

The calculated boundary layer is seen to become fully turbulent around a length Reynolds number ( $Rex$ ) of  $1 \times 10^6$ . The results for  $y^+ = 0.2$  and  $y^+ = 1$  are virtually identical indicating a grid independent solution. The  $y^+ = 5$  solution shows some small divergence from the  $y^+ = 1$  solution at the lower length Reynolds numbers while the  $y^+ = 10$  solution shows large differences from the other solutions.

Predicted velocity profiles for the flat plate boundary layer for various initial wall grid point spacings are shown in Fig. 4.5. The velocity profile shows little effect of the initial spacing for all but the  $y^+ = 10$  profile. All of the profiles but the  $y^+ = 10$  profile are in good agreement with the theoretical profile from Spalding. Note that the theoretical profile does not include the law-of-the wake (see Chapter 3), and hence the predicted profiles diverge from the theoretical profile in the wake region of the boundary layer. The predicted eddy viscosity for various initial wall spacings is shown in Fig. 4.6.

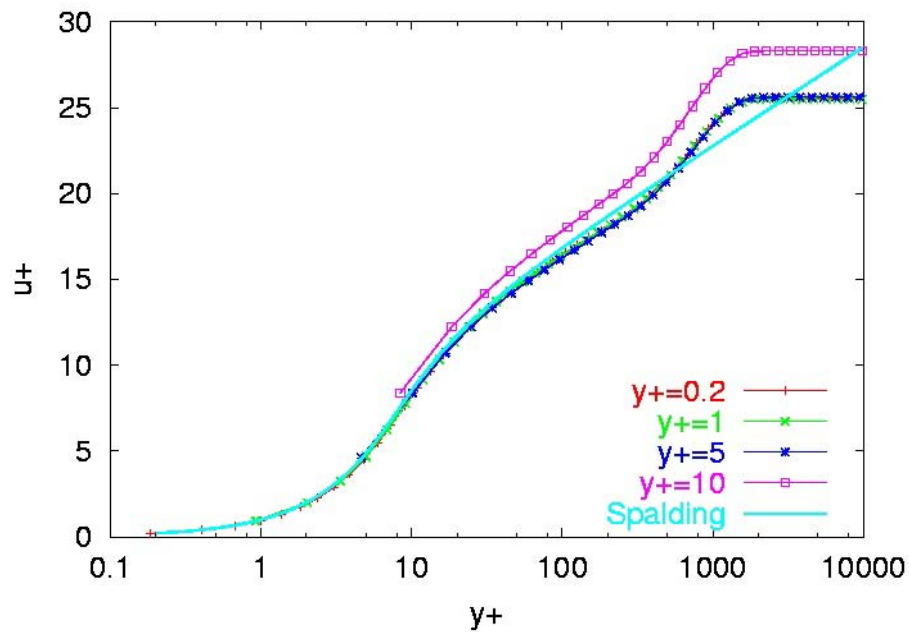


Figure 4.5 Flat plate boundary layer profiles predicted by the Baldwin-Lomax turbulence model for varying initial wall grid point spacings.

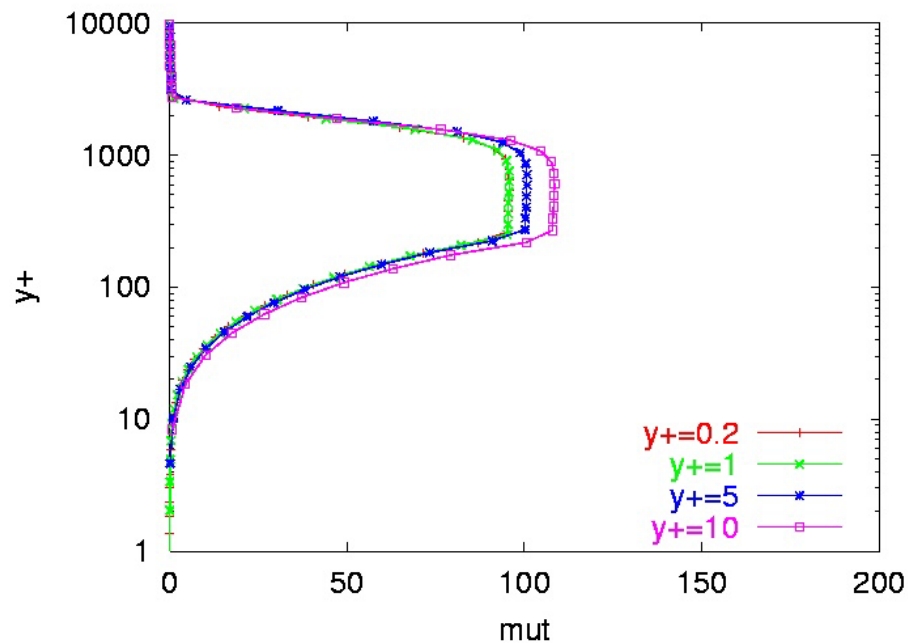


Figure 4.6 Eddy viscosity distribution predicted by the Baldwin-Lomax turbulence model for varying grid initial wall spacings.

Here again it is seen that the  $y^+=0.2$  and the  $y^+=1.0$  results are almost identical. The  $y^+=5$  and  $y^+=10$  results show the solutions are no longer grid independent at larger wall spacings.

The effect of grid stretching ratio on skin friction for a flat plate is shown in Fig. 4.7. All of these solutions used an initial wall spacing of  $y^+ = 1$ .

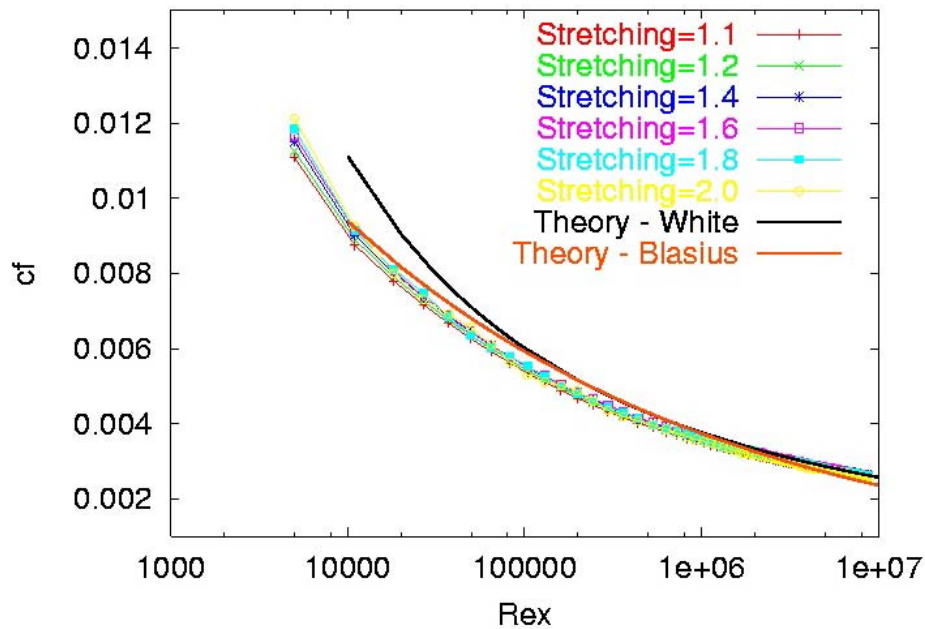


Figure 4.7 The effect of grid stretching ratio on the skin friction for a flat plate boundary layer using the Baldwin-Lomax turbulence model.

There seems to be very little effect of grid stretching for these cases, indicating that the initial wall spacing is the more critical parameter for skin friction predictions for flat plates with the Baldwin-Lomax turbulence model. This is also the case for the velocity profile, as seen in Fig. 4.8. The eddy viscosity does change as the stretching ratio increases, as shown in Fig. 4.9. It is interesting to note that a wide range of eddy viscosity distributions have little effect on skin friction and the velocity profile for a flat plate boundary layer. This insensitivity to the absolute eddy viscosity level is probably a major reason why the eddy viscosity concept has worked so well in practice.

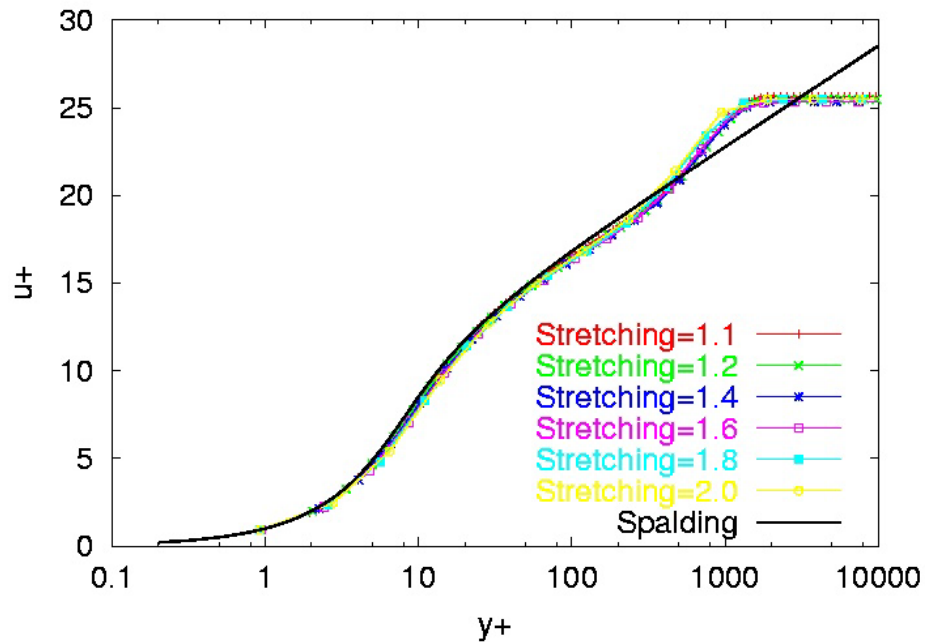


Figure 4.8 The effect of grid stretching ratio on the velocity profile for a flat plate boundary layer using the Baldwin-Lomax turbulence model.

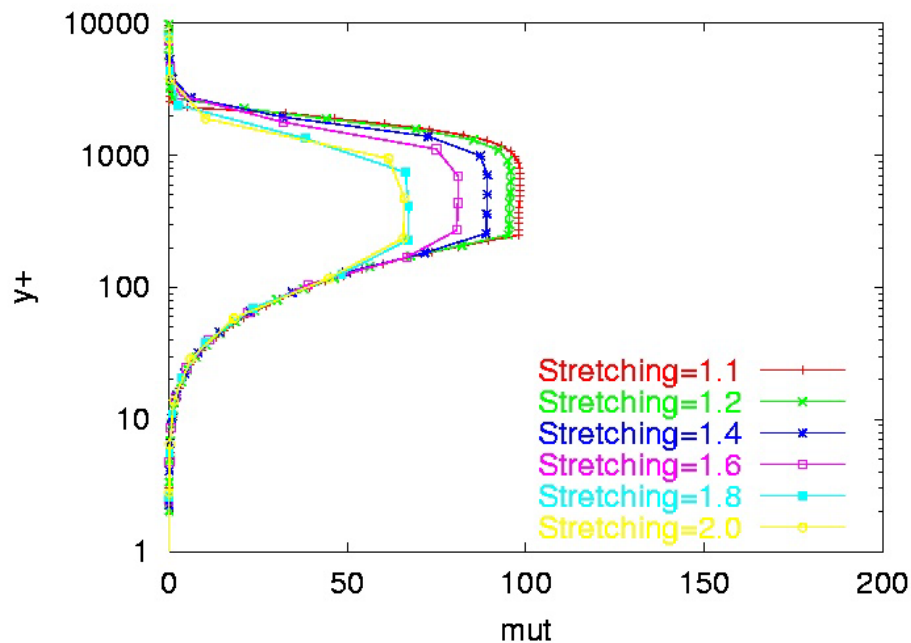


Figure 4.9 The effect of grid stretching ratio on the eddy viscosity distribution for a flat plate boundary layer using the Baldwin-Lomax turbulence model.

#### **4.7 Grid Sensitivity for Axisymmetric Bump**

A second example of the grid sensitivity of the Baldwin-Lomax turbulence model that includes a pressure gradient is the NASA Ames transonic axisymmetric

bump experiment (Ref. 7). The geometry is shown in Fig. 4.10. The model consisted of a sharp-lipped hollow cylinder with a 15.2 cm outer surface diameter. The bump was a circular arc 20.3 cm long and 1.9 cm high that begins 60.3 cm downstream of the cylinder leading edge. The upstream intersection of the bump and cylinder was faired with a circular arc. The test was run at a Mach number of 0.875 and a chord Reynolds number of  $2.67 \times 10^6$ .

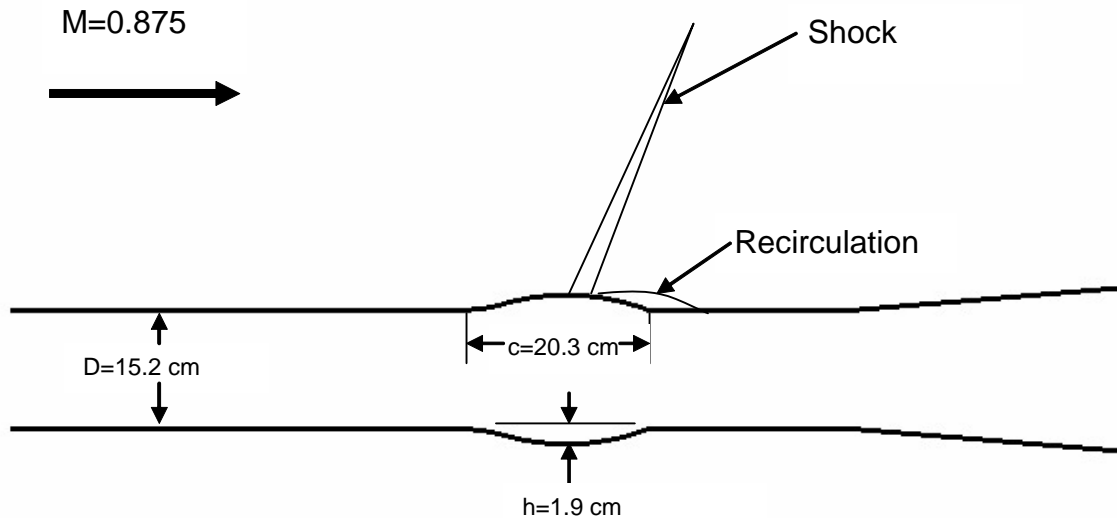


Figure 4.10 Geometry for the transonic axisymmetric bump.

The effect of initial grid spacing on the pressure coefficient distribution along the bump is shown in Fig. 4.11. The stretching ratio was 1.2 for these cases. The pressure coefficient seems to be relatively insensitive to the initial grid spacing, with the  $y^+=10$  and  $y^+=20$  curves being slightly displaced from the other curves. The velocity distribution at the aft junction of the bump and the cylinder ( $x/c=1$ ) is shown in Fig. 4.12. The  $y^+=20$  solution predicts a larger velocity in the reverse flow region than the other solutions. Grid stretching effects on the pressure coefficient distribution along the bump is shown in Fig. 4.13. The initial grid spacing was 1.2 for these cases. The pressure distribution coefficient changes slightly as the grid-stretching ratio is increased to 1.5. The solution in the separated region differs greatly for a grid-stretching ratio of 2.0. The effect on the velocity distribution at  $x/c=1$  is shown in Fig. 4.14. As with increasing initial grid spacing, increasing the grid spacing increases the size and the magnitude of the separated flow region.

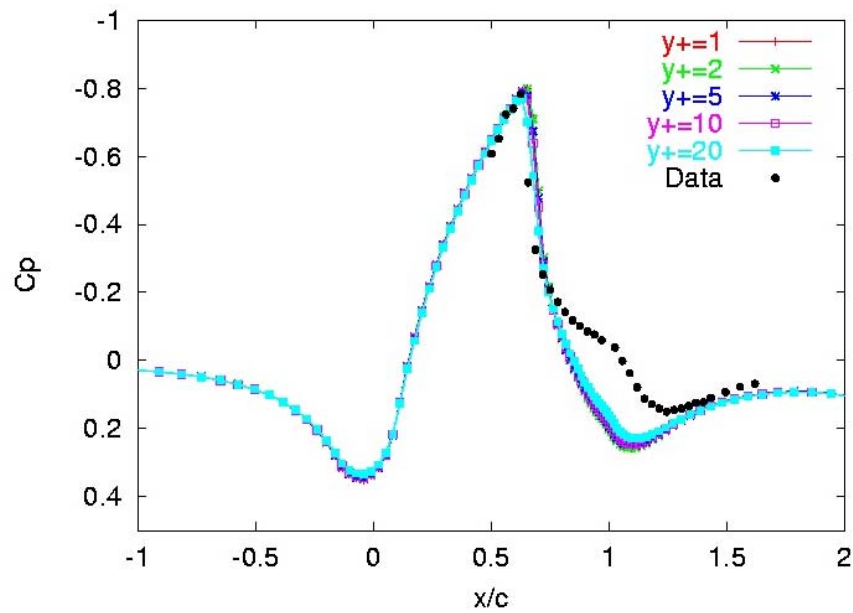


Figure 4.11 The effect of initial grid wall spacing on the pressure coefficient for the axisymmetric bump using the Baldwin-Lomax turbulence model.

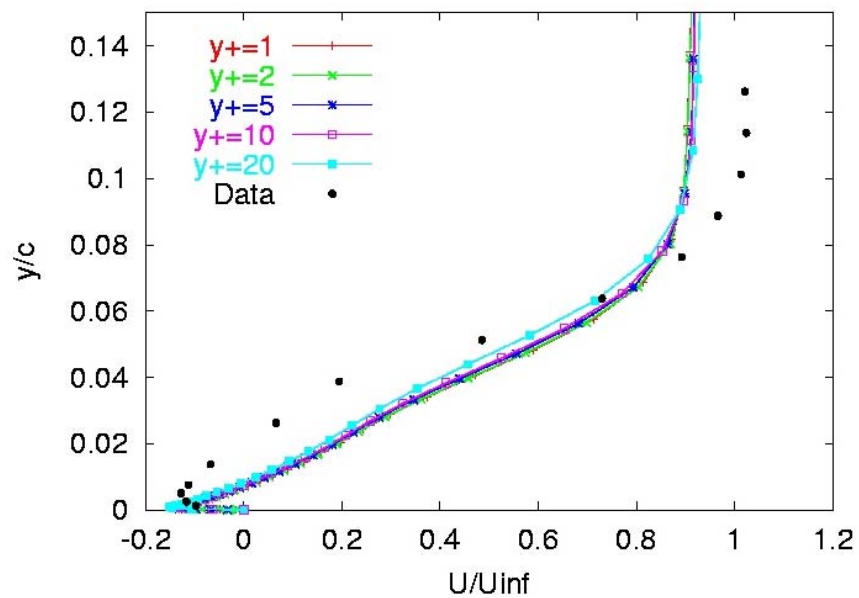


Figure 4.12 The effect of initial grid wall spacing on the velocity distribution at  $x/c=1$  for the axisymmetric bump using the Baldwin-Lomax turbulence model.

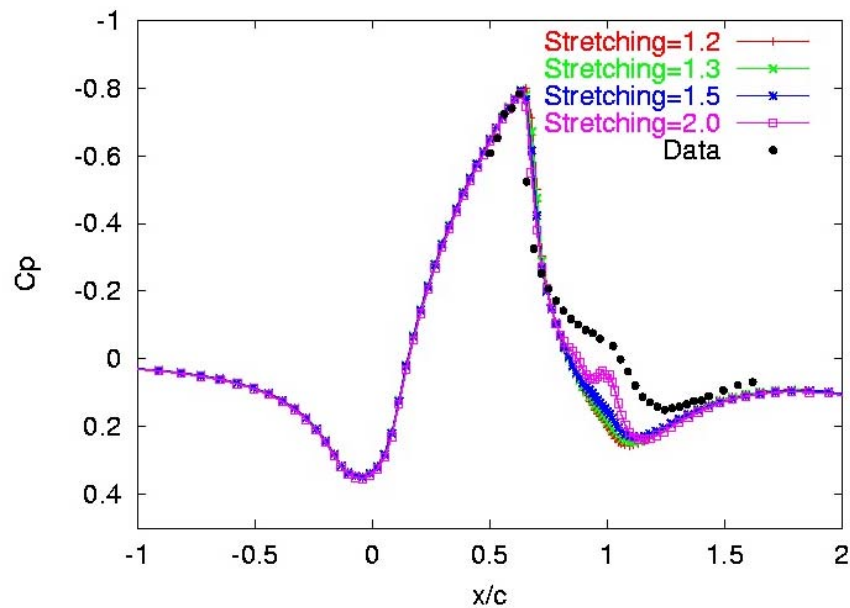


Figure 4.13 The effect of grid stretching on the pressure coefficient for the axisymmetric bump using the Baldwin-Lomax turbulence model.

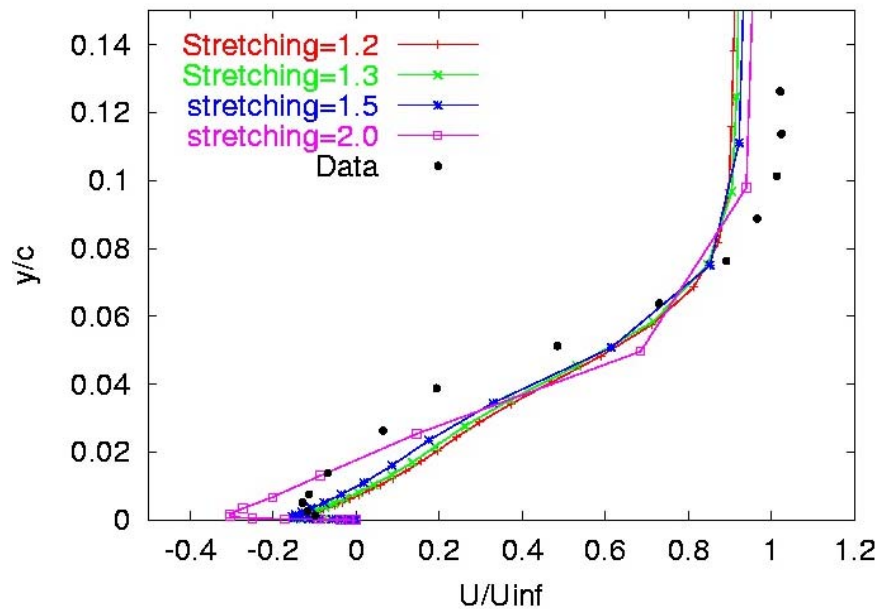


Figure 4.14 The effect of grid stretching on the velocity profile at  $x/c=1$  for the axisymmetric bump using the Baldwin-Lomax turbulence model.

The results for the Ames axisymmetric bump indicate that the grid-stretching ratio is a critical parameter when pressure gradients are present in the flow. The stretching ratio should probably be kept between 1.2 and 1.3 to assure that the grid can capture the pressure gradient effects. This is true in both structured and unstructured grids.

#### 4.8 Grid Sensitivity for a Flat Plate with Heat Transfer

Calculating heat transfer accurately can be more difficult than predicting skin friction. This can be seen in the subsonic flat plate example when the wall temperature is specified to be 1.5 times the free-stream temperature. The sensitivity of the skin friction and heat transfer result with varying initial grid wall spacing is shown in Fig. 4.15 and Fig. 4.16. The grid stretching ratio was fixed at 1.2 for these results. Both the skin friction and heat transfer seem to be relatively insensitive to the wall spacing for wall spacings less than  $y^+ = 5$  when no pressure gradient is present.

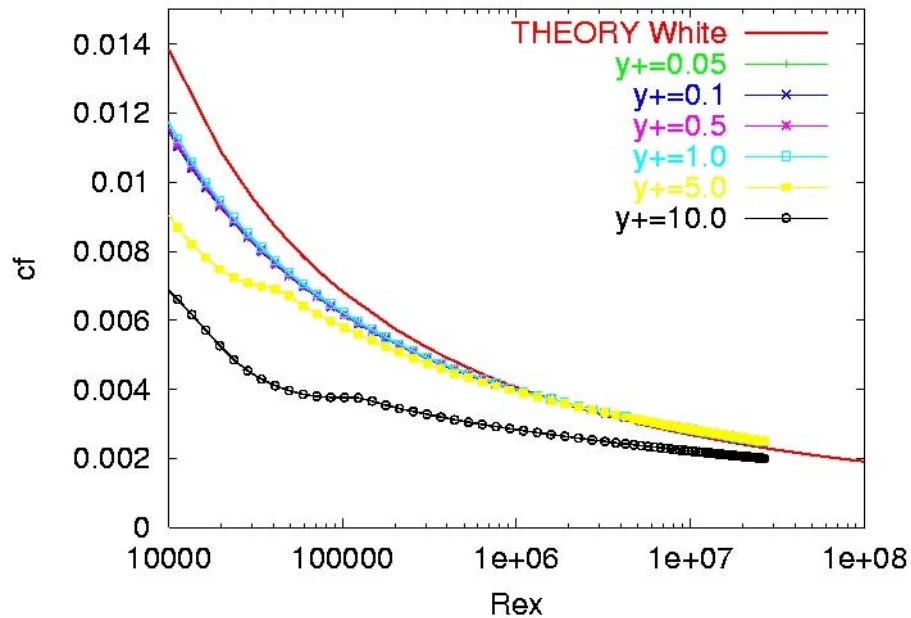


Figure 4.15 The effect of wall spacing on the skin friction on a flat plate with heat transfer using the Baldwin-Lomax turbulence model.

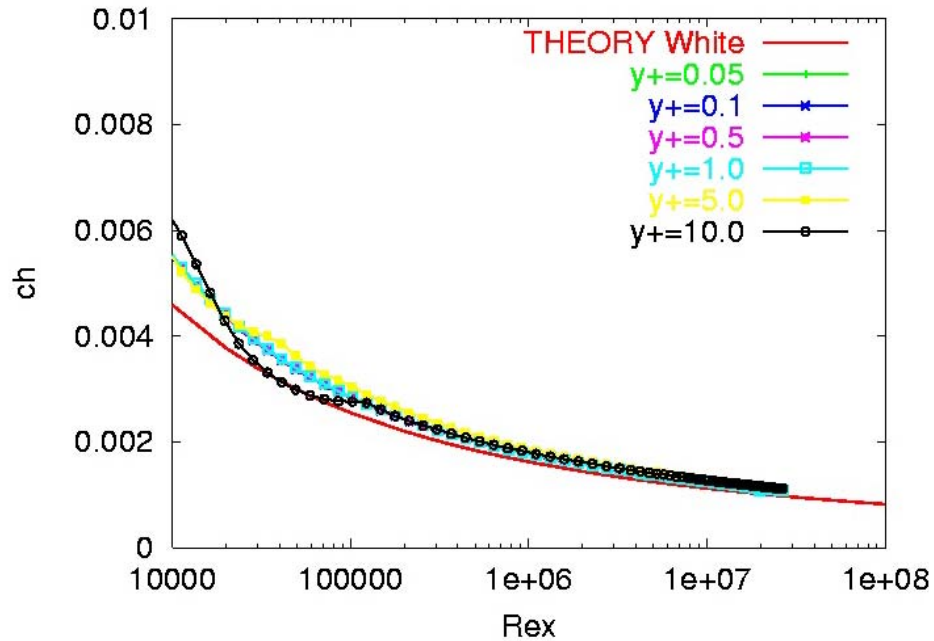


Figure 4.16 The effect of wall spacing on the heat transfer (Stanton number) on a flat plate using the Baldwin-Lomax turbulence model.

The velocity and temperature profiles for a length Reynolds number ( $Re_x$ ) of  $1.0 \times 10^7$  are shown in Fig. 4.17 and 4.18 respectively. Both the velocity and temperature profiles are relatively insensitive to wall spacing for this model when no pressure gradient is present.

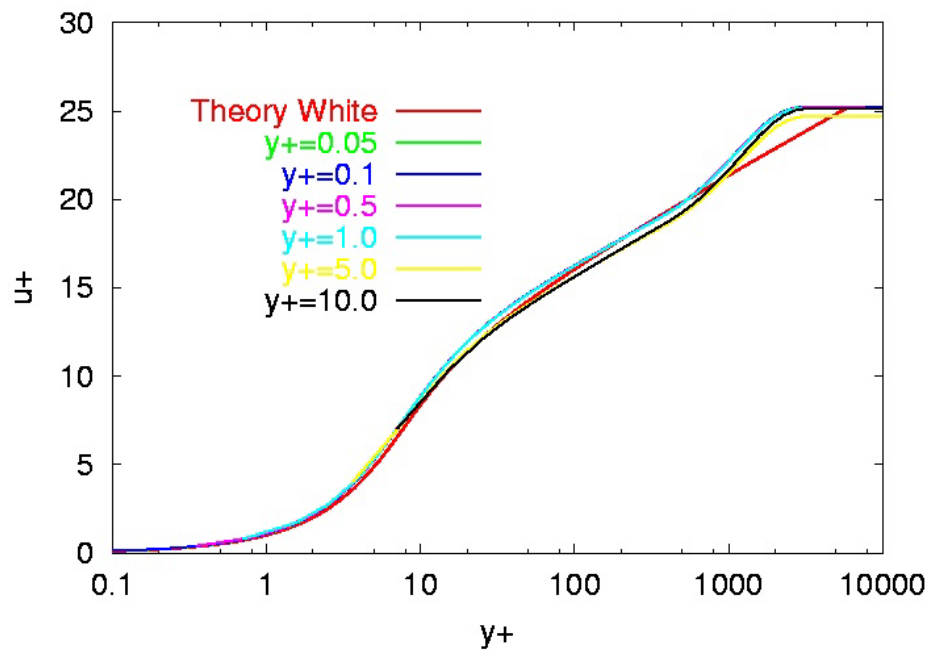


Fig. 4.17 The effect of wall spacing on the velocity profile on a flat plate with heat transfer using the Baldwin-Lomax turbulence model.

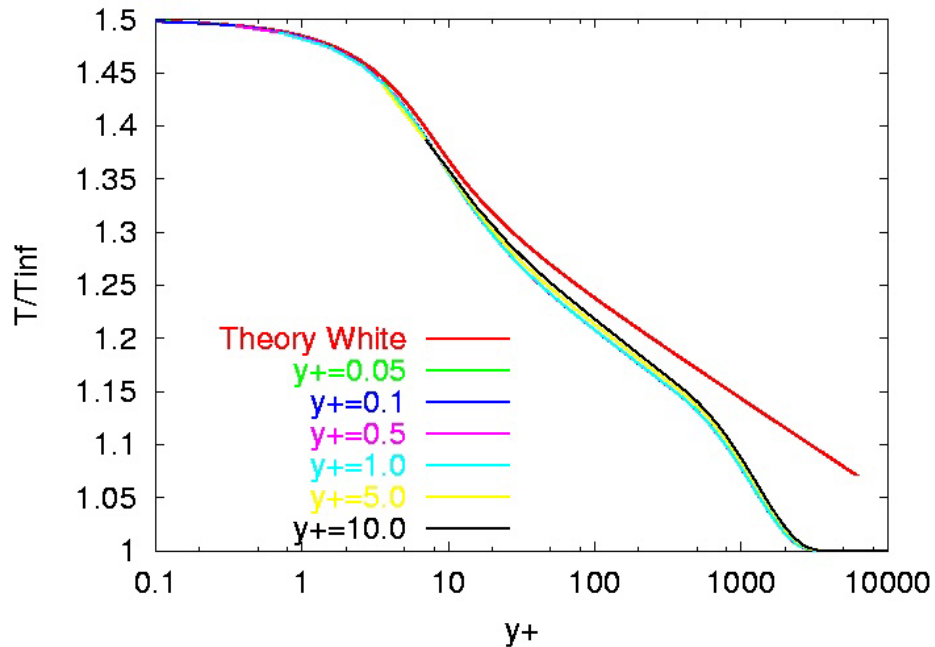


Fig. 4.18 The effect of wall spacing on the temperature profile on a flat plate with heat transfer using the Baldwin-Lomax turbulence model.

Grid stretching effects on skin friction and heat transfer predictions are shown in Fig. 4.19 and 4.20. The effect of grid stretching on the velocity and temperature profiles are shown in Fig. 3.22 and 3.23 respectively. The initial wall spacing was held at  $y^+ = 0.1$  for these calculations. The results reach a grid independent result for a stretching ratio of less than 1.3.

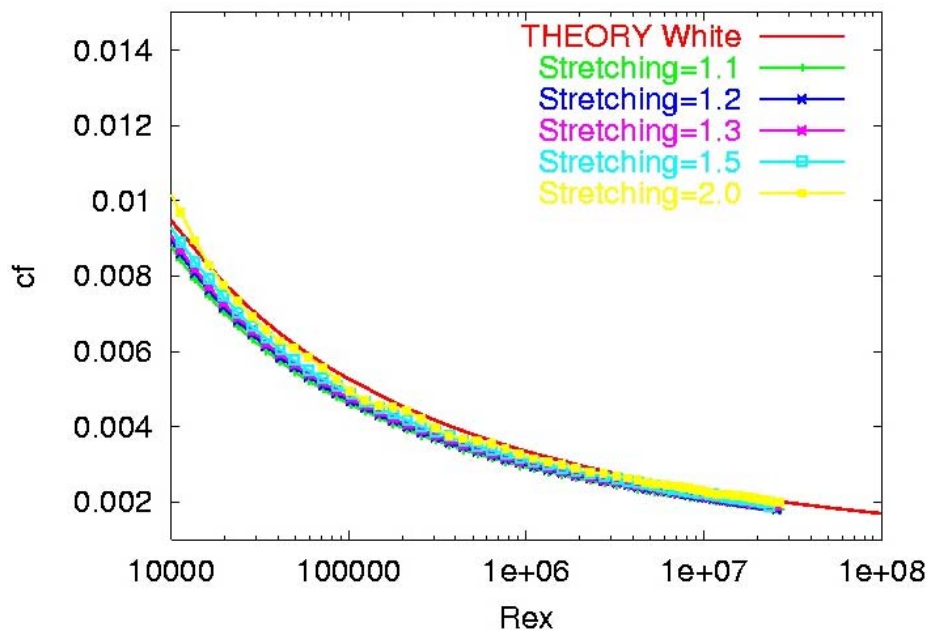


Figure 4.19 The effect of grid stretching on the skin friction on a flat plate with heat transfer using the Baldwin-Lomax turbulence model.

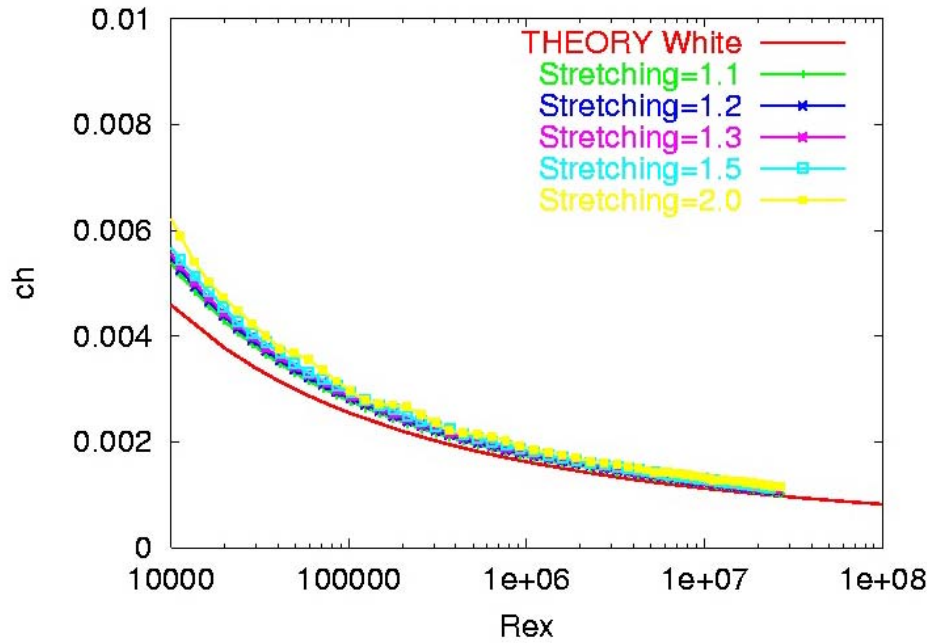


Figure 4.20 The effect of grid stretching on heat transfer (Stanton number) on a flat plate using the Baldwin-Lomax turbulence model.

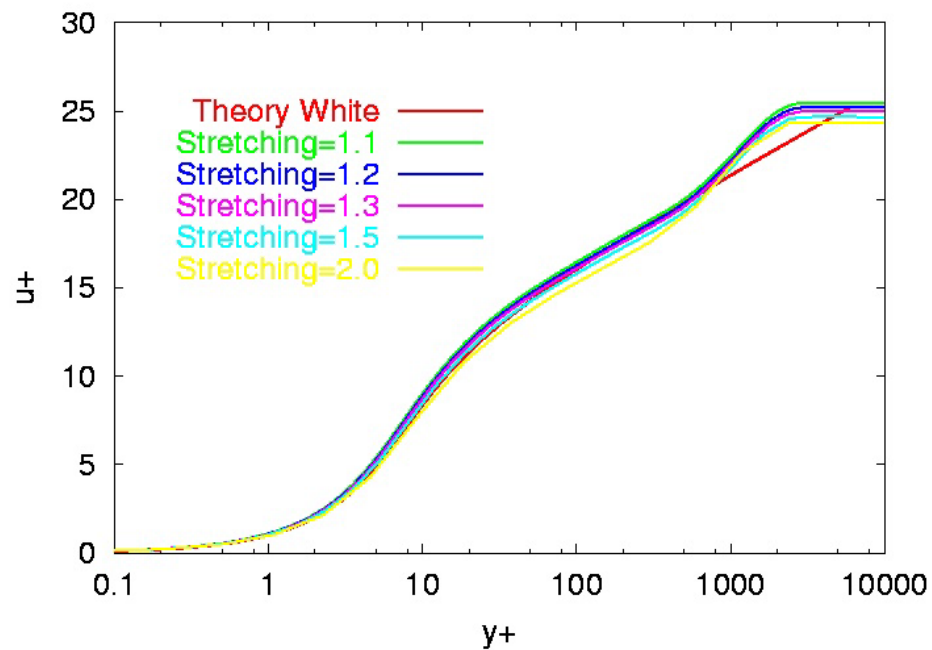


Figure 4.21 The effect of grid stretching on the velocity profile on a flat plate with heat transfer using the Baldwin-Lomax turbulence model.

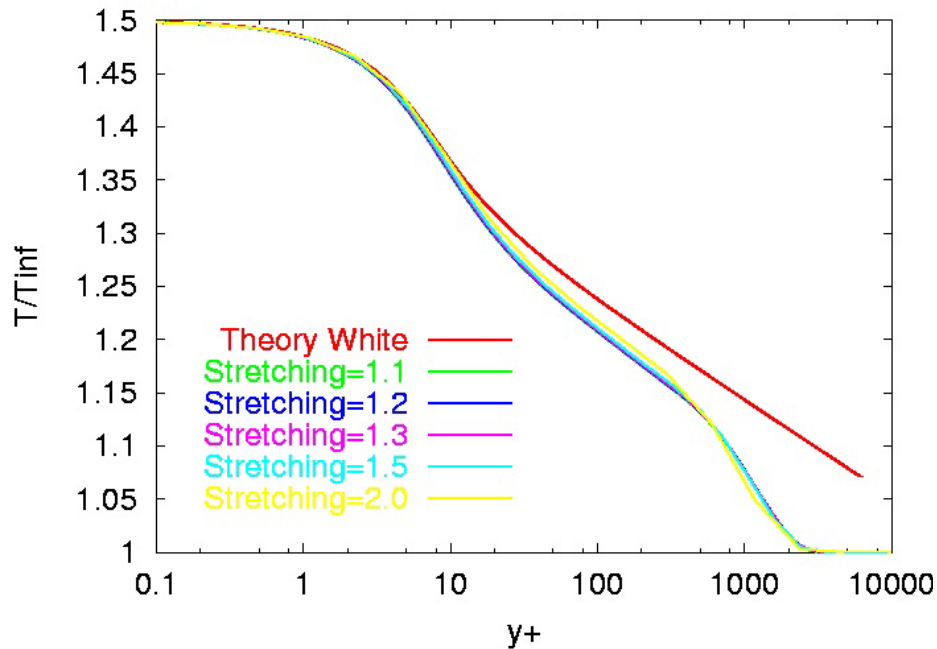


Figure 4.22 The effect of grid stretching on the temperature profile on a flat plate with heat transfer using the Baldwin-Lomax turbulence model.

#### 4.9 Grid Sensitivity for a Nozzle with Heat Transfer

Flow through a supersonic nozzle with a constant temperature wall can serve as a test case for evaluating the performance of the turbulence model in the presence of strong pressure gradients. Back, Massier, and Gier<sup>8</sup> measured the wall pressure distribution and heat transfer for a converging-diverging nozzle with a throat diameter of 0.0458 meters and an exit diameter of 0.1227 meters. High-pressure air was heated by the internal combustion of methanol and flowed along a cooled constant area duct with a length of 0.4572 meters and a diameter of 0.355 meters before entering the nozzle. The nozzle geometry and boundary conditions are shown in Fig. 4.23. The gas could be treated as a calorically perfect gas with a ratio-of-specific heats ( $\gamma$ ) of 1.345. The nozzle exit Mach number was approximately 2.5. The molecular viscosity and thermal conductivity were assumed to vary according to Sutherland's law.

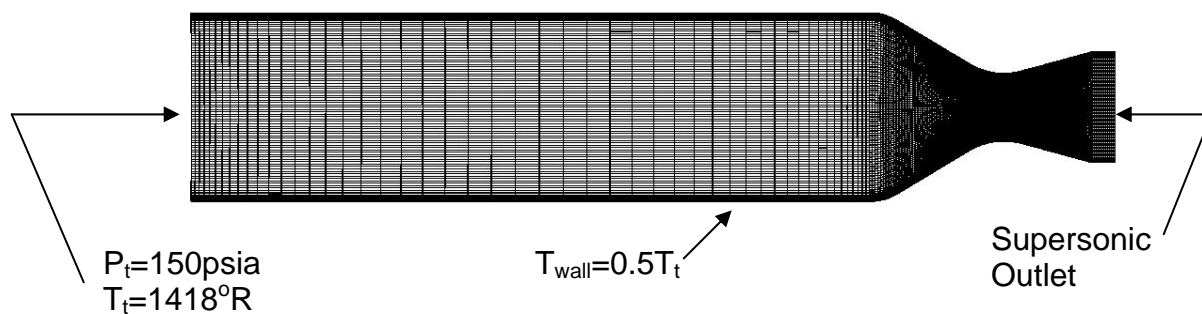


Figure 4.23 Nozzle geometry.

The initial wall spacing was varied with a grid stretching ratio of 1.2 in the boundary layer. The grid spacing was held constant in the core of the nozzle. Comparisons of the predicted and measured pressure along the nozzle are shown in Fig. 4.24 for varying initial wall spacings. The throat is located at  $x=0.091$  meters. The pressure distribution is seen to be insensitive to the initial wall spacing. The heat transfer at the wall is shown in Fig. 4.25. The results are in poor agreement with the data and are quite sensitive to the initial wall spacing, especially for wall spacing greater than  $y+=1$ .

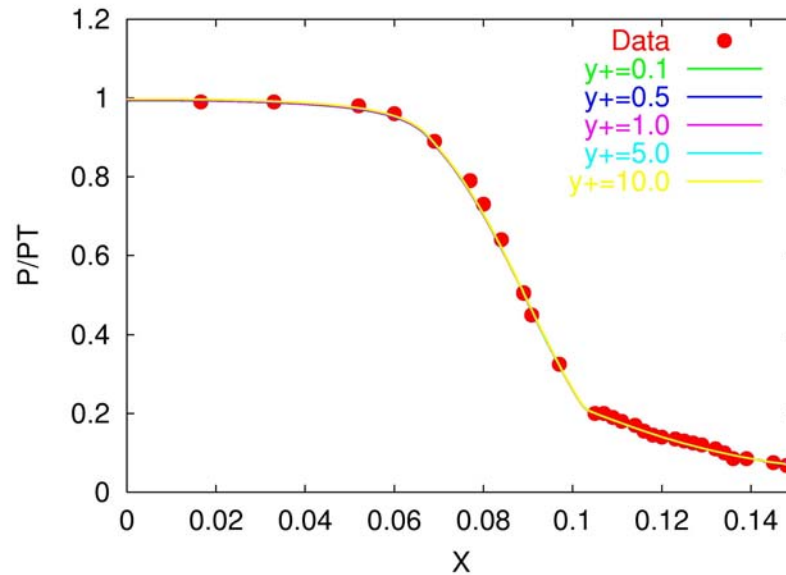


Figure 4.24 The effect of wall spacing on the pressure distribution for a supersonic nozzle with heat transfer using the Baldwin-Lomax turbulence model.

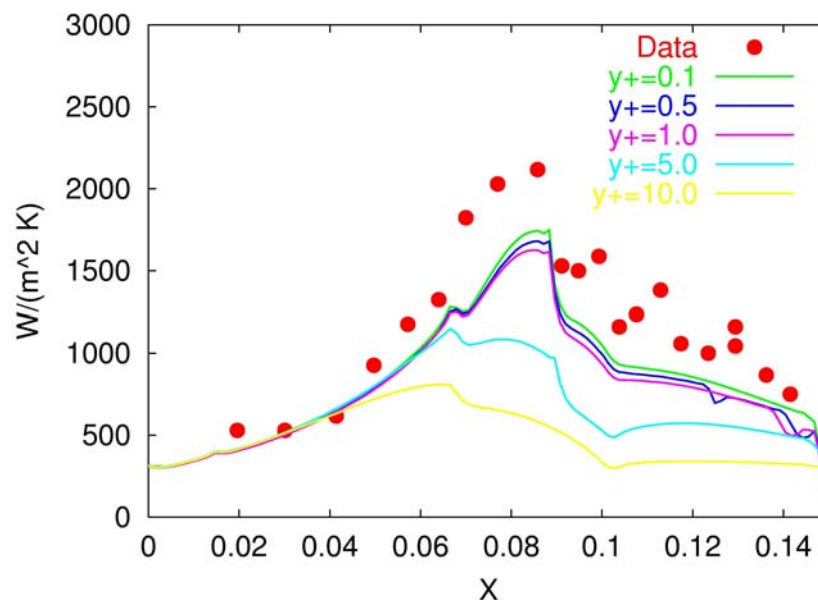


Figure 4.25 The effect of wall spacing on the wall heat transfer distribution for a supersonic nozzle using the Baldwin-Lomax turbulence model.

The poor performance of the Baldwin-Lomax model for this case is due to the difficulty in choosing the proper  $F_{max}$  peak as was described in Section 4.5. The  $F$  function at the nozzle throat is shown in Fig. 4.26. Notice that multiple peaks are present in the function. It is extremely difficult to predict which, if any, of these three peaks is the proper value for this case. The eddy viscosity distribution at the nozzle throat is shown in Fig. 4.27. The Spallart-Allmaras eddy viscosity distribution is included in Fig. 4.26 for comparison. The Baldwin-Lomax eddy viscosity is much lower than the Spalart-Allmaras distribution and is seen to cut off prematurely. This low value of eddy viscosity results in a low prediction of the wall heat transfer.

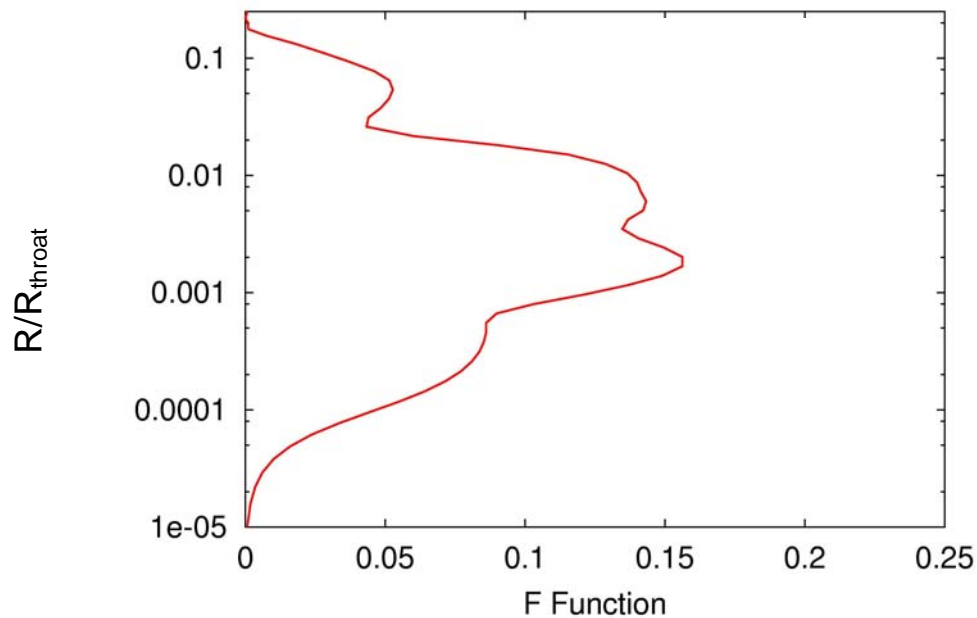


Figure 4.26 The  $F$  function at the nozzle throat.

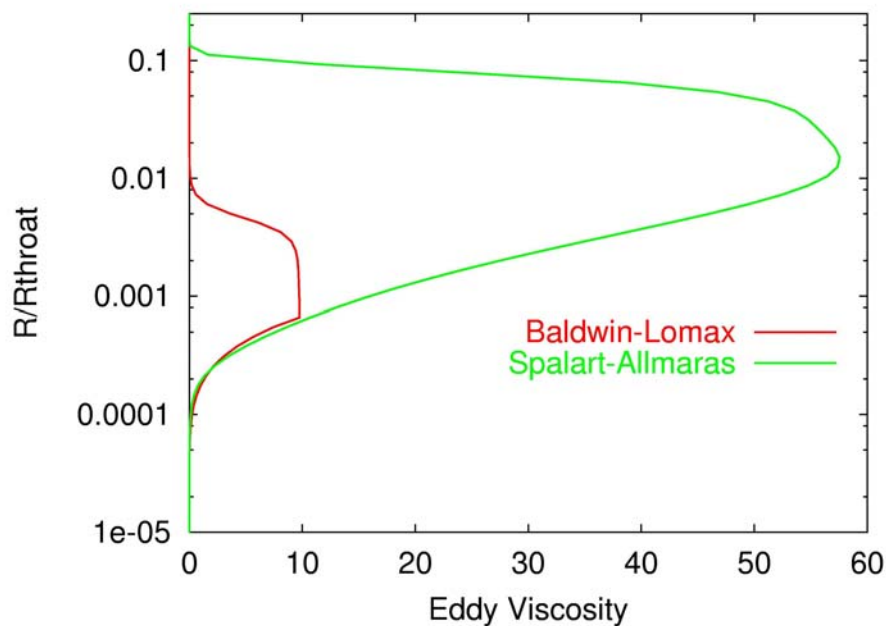


Fig. 4.27 The eddy viscosity distribution at the nozzle throat.

#### **4.10 Summary**

Algebraic turbulence models were popular in the 1970's and 1980's because of their simplicity and robustness. As Navier-Stokes CFD applications became more complex in the 1990's these models began to lose popularity because of accuracy limitations for flows that contain multiple shear layers or boundary layer separation. The difficulties encountered when multiple peaks occur in the  $F$  function have been demonstrated. These models have also lost favor in unstructured grid applications since they require a velocity profile over multiple grid points aligned with the flow for successful application.

The eddy viscosity predicted by an algebraic turbulence model is only a function of the local velocity profile used to generate the  $F$  function. Thus the eddy viscosity relates directly to the local instantaneous vorticity field of that profile and cannot model the transport of turbulence by the flow. This makes these models a poor choice for unsteady flows and for flows where turbulent transport is important.

### Baldwin-Lomax Application Hints

1. The Baldwin-Lomax model requires that the  $F$  function be well defined. This normally requires that at least three points be located within the sublayer ( $y^+ < 10$ ). The first point off the wall should be located about  $y^+ < 5$  for pressure distributions,  $y^+ < 2$  to obtain reasonable skin friction values, and  $y^+ < 0.5$  for heat transfer. The grid stretching normal to the wall should not exceed 1.3. Improved heat transfer results can be obtained by using a constant spacing for the first three cells off the wall.
2. In order to reduce the probability of finding a second peak well off the wall, it is usually good to limit the number of points over which the  $F$  function is calculated.
3. Care should be taken not to divide viscous regions such as boundary layers when dividing the computational domain for blocked or chimera applications since the entire velocity profile is required to properly define the  $F_{max}$  and  $U_{diff}$  quantities.

### **Chapter 4 References:**

1. Prandtl, L., "Bericht uber Untersuchungen zur Ausgebildeten Turbulenz," *Z. Angew Math.*, Meth., Vol. 5, pp. 136-139.
2. Cebeci, T, and Smith, A. M. O., Analysis of Turbulent Boundary Layers, Academic Press, New York, 1974.
3. Baldwin, B. S. and Lomax, H., "Thin Layer Approximation and Algebraic Model for Separated Turbulent Flows," AIAA-78-0257, Jan. 1978.
4. Klabenoff, P. S., "Characteristics of Turbulence in a Boundary Layer with Zero Pressure Gradient," NACA Rep. 1247, 1955.
5. Degani, D. and Schiff, L. B., "Computation of Supersonic Viscous Flows Around Pointed Bodies at Large Incidence," AIAA-83-0034, Jan. 1983.
6. Buning, P. G., Jespersen, D. C., Pulliam, T. H., Klopfer, G. H., Chan, W. C., Slotnik, J. P., Krist, S. E., and Renze, K. J., "OVERFLOW User's Manual," Version 1.8I, July 1999.
7. Johnson, D. A., "Predictions of Transonic Separated Flow with an Eddy-Viscosity/Reynolds Shear Stress Closure Model," AIAA-85-1683, July 1985.
8. Back, L. H., Massier, P. F., and Gier, H. L., "Convective Heat Transfer in a Convergent-Divergent Nozzle," *International Journal of Heat Mass Transfer*, Vol. 7, 1964, pp. 549-568.